



HAL
open science

Phase diagram and thermo-elastic properties of Fe-S compounds up to 15 GPa: Thermodynamic constraints on the core of medium-sized telluric planets

Bin Zhao, Guillaume Morard, Silvia Boccato, Mohamed Mezouar, Daniele Antonangeli

► To cite this version:

Bin Zhao, Guillaume Morard, Silvia Boccato, Mohamed Mezouar, Daniele Antonangeli. Phase diagram and thermo-elastic properties of Fe-S compounds up to 15 GPa: Thermodynamic constraints on the core of medium-sized telluric planets. *Earth and Planetary Science Letters*, 2024, 634, pp.118676. 10.1016/j.epsl.2024.118676 . hal-04523329

HAL Id: hal-04523329

<https://hal.science/hal-04523329>

Submitted on 27 Mar 2024

HAL is a multi-disciplinary open access archive for the deposit and dissemination of scientific research documents, whether they are published or not. The documents may come from teaching and research institutions in France or abroad, or from public or private research centers.

L'archive ouverte pluridisciplinaire **HAL**, est destinée au dépôt et à la diffusion de documents scientifiques de niveau recherche, publiés ou non, émanant des établissements d'enseignement et de recherche français ou étrangers, des laboratoires publics ou privés.

1 **Phase diagram and thermo-elastic properties of Fe-S compounds up to 15 GPa:**
2 **thermodynamic constraints on the core of medium-sized telluric planets**

3
4 Bin Zhao^{1*}, Guillaume Morard², Silvia Boccato¹, Mohamed Mezouar³ and Daniele
5 Antonangeli¹

6
7 ¹Sorbonne Université, Muséum National d'Histoire Naturelle, UMR CNRS 7590, Institut de
8 Minéralogie, de Physique des Matériaux et de Cosmochimie, IMPMC, 75005 Paris, France

9
10 ²Université Grenoble Alpes, Université Savoie Mont Blanc, CNRS, IRD, Université Gustave
11 Eiffel, ISTERre, 38000 Grenoble, France

12
13 ³European Synchrotron Radiation Facility, Boîte Postale 220, 38043 Grenoble, France

14
15 ^{*}Now at Institute for planetary materials, Okayama University, Misasa 682-0193, Japan

16
17 Keywords: Iron-sulfur alloys, planetary cores, high pressure and high temperature, phase
18 transition, equation of state

19
20 Abstract

21
22 The Fe-FeS binary is largely seen as the archetypal system to model the properties of
23 the core of small to medium-sized telluric planetary bodies. Noteworthy, while both at
24 the low pressures characteristic of the Moon, and at the very high pressure pertinent to
25 the Earth or Venus, the Fe-FeS is a simple binary eutectic, in the intermediate range
26 relevant for planets such as Mercury or Mars, or satellite such as Ganymede,
27 Io, and Europa, the Fe-S phase diagram is quite complex, with intermediate
28 compounds of narrow stability field that incongruently melt.

29 Properties of Fe-FeS compounds have been here studied using *in situ* X-ray
30 diffraction in the pressure range of 11-15 GPa, between room temperature to solidus
31 (around ~1100 K). Results show that Fe + FeS mixture transforms to Fe₃S₂ at 850 K
32 and 12.1 GPa, adopting an orthorhombic crystal structure. Fitting the unit-cell
33 volumes at 940 K to 2nd order Birch-Murnaghan and Vinet equation of state yields to
34 $V_0=372.2 \pm 0.8$ or $367.3 \pm 0.6 \text{ \AA}^3$ and $K_0=130 \pm 4$ or 185 ± 4 GPa, respectively, with
35 K' fixed to 4. The thermal expansion around 14 GPa has been estimated to be
36 $26.6 \times 10^{-5} \text{ K}^{-1}$ based on the temperature evolution of the unit-cell volume from 850 K
37 to 1100 K. Moreover, the lattice parameters of FeS were obtained in the range 11-15
38 GPa between 470 K and 1100 K, and the compressional behavior was studied.

39 To model the properties of the solid portion of the cores of telluric planets or
40 exoplanets in the 12-21 GPa range, Fe₃S₂ should be used as the end-member together
41 with Fe or FeS depending on whether the S content is below or above 27 wt%. While
42 Fe₃S₂ is a potential crystallizing product of S-rich telluric bodies, it is not expected to
43 form in the core of Europa, Io, or Ganymede as too small, nor in that of Mercury as
44 most likely too poor in S. When found in a meteorite, the Fe₃S₂ phase could be used

45 to infer the size and temperature of the parent body.

46

47 1. Introduction

48

49 Small and medium-sized terrestrial planetary bodies in the solar system, going from
50 satellites such as the Moon, Ganymede, Io, and Europa, to planets such as Mercury
51 and Mars, are considered to have a core less dense than pure iron, indicating the
52 presence of light elements (e.g. Anderson et al., 1996a, 1996b, 1998, 2001; Hussmann
53 et al., 2016; Morard et al., 2018; Rivoldini et al., 2009, 2011; Stähler et al., 2011). The
54 potential light elements, depending on the nature of the material that accreted to form
55 the planet as well as the physical conditions during planetary differentiation (e.g.
56 Pommier et al., 2022), include H, O, Si, C, and S. In the case of the Moon and Mars,
57 available seismic records have been exploited to propose core composition on the
58 basis of density and sound velocities (e.g. Antonangeli et al., 2015; Irving et al., 2013;
59 Weber et al., 2011). In all other cases, more indirect constraints come from the models
60 developed to account for the overall limited observables collected by orbiters, such as
61 the MESSENGER mission to Mercury and the Galileo mission for what concerns the
62 Galilean moons of Jupiter (e.g. Rivoldini et al., 2011; Smith et al., 2012; Kivelson et
63 al., 1996). In the large majority of these models, out of the above-cited list, sulfur is
64 considered the most plausible light element, as it is highly siderophile under planetary
65 pressure (P) and temperature (T) core conditions, and because Fe-S compounds are
66 widespread in Fe meteorites (Jones and Drake, 1983; Fei et al., 1995). Therefore, the
67 phase diagram of the Fe-FeS system and the thermo-elastic properties of the stable
68 phases under relevant P-T conditions have sparked significant interest as they play a
69 crucial role in modeling the current status, composition, and crystallization regime
70 during secular cooling of the core of terrestrial bodies.

71

72 The Fe-FeS system evolves with increasing pressure from a simple binary eutectic at
73 the pressure conditions of the Moon's core (~5 GPa) to a more complex diagram at
74 pressures above 10 GPa (Buono and Walker, 2011; Fei et al., 1997, 2000), with
75 intermediate compounds of narrow and yet undetermined stability field, that
76 incongruently melt. For instance, Fe₃S₂ was found in recovered samples from
77 quenched experiments above 14 GPa by Fei et al. (1997) and Koch-Müller et al.
78 (2002) and observed as an intermediate phase coexisting with Fe or FeS below 21
79 GPa (Fei et al., 1997), but actual P-T phase boundaries and stability field are largely
80 unconstrained. Structure and equation of state (EOS) are also unknown. When in
81 coexistence with Fe, Fe₃S₂ is reported to transform into Fe₃S around 21 GPa (Fei et al.,
82 2000), which has a tetragonal crystal structure (space group $\bar{I}4$) stable up to ~250 GPa
83 (Morard et al., 2008; Ozawa et al., 2013; Mori et al., 2017). At even higher pressure,
84 Fe₃S is replaced by Fe₂S, adopting an orthorhombic structure (space group *Pnma*),
85 which remains stable up to 306 GPa and 3000 K (Tateno et al., 2019). Very recently, a
86 novel phase, Fe₅S₂ (with hexagonal structure in the space group *P63_cm*) was reported
87 to form from high-temperature decomposition of Fe₃S above 120 GPa (Zurkowski et
88 al., 2022).

89

90 As outlined above, while many recent studies have focused on the high-pressure Fe-S
91 phases targeting the conditions corresponding to those of Earth's core, the stability
92 field and the crystallographic structure of the moderate-pressure phase Fe₃S₂ has
93 remained undetermined, making it a potential candidate material for the core of small
94 to medium-sized planetary bodies, including e.g., Ganymede, Io and Europa, and
95 portion of the core of Mercury and potentially Mars. As well, the Fe-FeS phase
96 diagram turned out to be more complex with the appearance of Fe₃S₂, and current
97 thermodynamic models lack in reliability due to the undefined stability field of this
98 intermediate compound.

99 To address these questions, we have conducted *in situ* X-ray diffraction experiments
100 on Fe-FeS mixtures up to 15 GPa and 1200 K using a Paris-Edinburgh press to
101 specifically investigate the P-T stability range, structure, and EOS of Fe₃S₂.

102

103

104 2. Materials and methods

105

106 The starting materials are iron (99.5%, Alfa Aesar) and iron sulfide (FeS) powders
107 (99.98%, Alfa Aesar). These powders were mixed into four nominal compositions:
108 Fe-15 wt%S (hereafter referred to as Fe-15S), Fe-20S, Fe-25S, and Fe-30S. These
109 compositions encompass the stoichiometric Fe₃S₂, which contains 27.7 wt% of sulfur.
110 Mixed powders were ground in an agate mortar for 30 min and then dehydrated and
111 stored in a vacuum box to minimize the risk of contamination.

112

113 The powder samples were loaded into an hBN capsule for experiments. The pressure
114 was generated by a VX5-type Paris-Edinburgh press (Morard et al., 2011), equipped
115 with a pair of sintered diamond anvils. The experimental setup included a 5/1.5 mm
116 assembly consisting of a boron epoxy gasket, a graphite furnace, an hBN capsule, and
117 several electron-conducting disks and rings, similar to the one described in Morard et
118 al. (2007) and Boulard et al. (2020). For more details, please refer to Figure S1 of the
119 Supplementary.

120

121 *In situ* angle dispersive X-ray diffraction experiments were conducted at the ID27
122 beamline of European Synchrotron Radiation Facility (ESRF) in Grenoble, France.
123 The incoming beam energy was selected by a Si(111) channel cut monochromator to
124 33.17 keV (Iodine K-edge) and the beam size was then collimated to 50 μm×50 μm
125 FWHM. A double-layer Soller Slits system located between the sample and the
126 detector allows efficiently filtering out the background signal from the environment
127 (Morard et al., 2011). The diffracted beam going through the Soller Slits was collected
128 by a Pilatus CdTe 3M detector, with an exposure time of 30 s. Pressure and
129 temperature during experiments were determined *in situ* by the cross calibration of the
130 EOS of MgO and NaCl, exploiting the MgO serving as the lid on the capsule and
131 NaCl powder mixed in the samples (see Zhao et al., 2023 and references therein). The
132 P-T conditions estimated by this protocol come with an uncertainty of ±100 K on the

133 temperature, including the potential temperature gradient within the cell, and ± 0.6
134 GPa on the pressure.

135

136 Samples were first cold compressed to the target pressure, and then heated.
137 Angle-dispersive X-ray diffraction patterns from $2\theta = 0.005^\circ$ to 21° , with a resolution
138 of 0.0038° , were taken on the sample and calibrants for increasing temperature at
139 steps of 20 W (power applied to the heating furnace), until melting. Diffraction
140 patterns were processed by Dioptas (Prescher and Prakapenka, 2015). Lattices of
141 Fe_3S_2 and other components in the sample were indexed by DICVOL (Boultif and
142 Louer, 1991). After quench, a polished section of the recovered samples was studied
143 by a ZEISS Supra 55VP scanning electron microscope (SEM), equipped with an
144 energy dispersive spectroscopy (EDS) detector, at IStEP, Sorbonne Université.

145

146

147 3. Results

148

149 3.1 Experimental paths and products

150

151 The experiments include four high-temperature runs around 13 GPa, one on each
152 composition. An isothermal decompression at 940 K was performed from 14.2 GPa
153 on Fe-20S to investigate the phase stability of Fe_3S_2 . One further heating run on
154 Fe-25S was performed at around 11 GPa to further constrain the lower pressure
155 boundary of Fe_3S_2 . Figure S2 shows the P-T paths followed in the various
156 experiments before quenching.

157

158 Table 1 shows the maximum pressure and temperature that have been reached in each
159 run and the corresponding products identified by *in situ* XRD. The appearance of
160 Fe_3S_2 was identified by the appearance of a large number of new peaks observed
161 around 870 K in all high-pressure runs (see for instance heating run on Fe-15S, left
162 panel of Figure 1). Trace amounts of FeO were detected around 680 K before the
163 Fe_3S_2 was produced, likely a consequence of oxidation of iron in contact with the
164 MgO P-T calibrant. Similar iron oxidation was already reported by Deng et al. (2013)
165 where MgO capsules were adopted. This explains the anomalous products from the
166 run on Fe-25S, where the expected products were Fe and Fe_3S_2 , while FeS and Fe_3S_2
167 were detected by the XRD due to the partial oxidation of initial Fe into FeO.

168

169

170 Table 1 Maximum P, T and products of each run

Run	P_{\max} (GPa)	T_{\max} (K)	Products
Fe-15S	15.0	1110 ^a	Fe+ Fe_3S_2 + trace FeO ^b
Fe-20S	14.2 (Decompressed to 12.1)	940 (Kept at 940)	Fe+ Fe_3S_2 + trace FeO (Fe+FeS + trace FeO)
Fe-25S (low-P)	12.0	1100 ^a	Fe+FeS + trace FeO ^b

Fe-25S (high-P)	15.0	910	FeS+Fe ₃ S ₂ + trace FeO
Fe-30S	14.9	920	FeS+Fe ₃ S ₂ + trace FeO

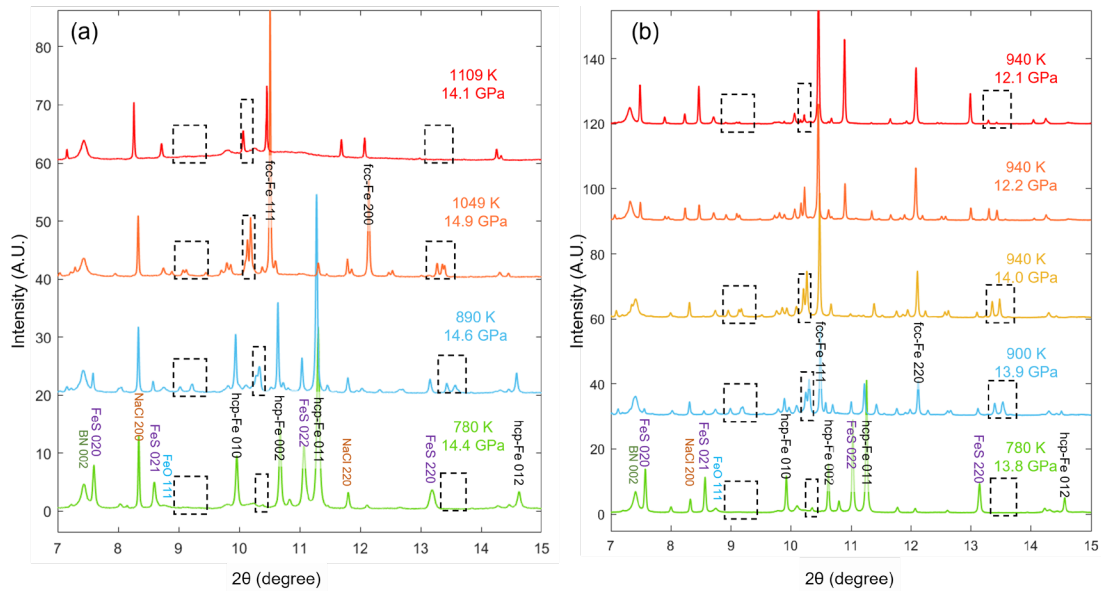
171

^a Partial melting.

172

^b Observed already before melting

173



174

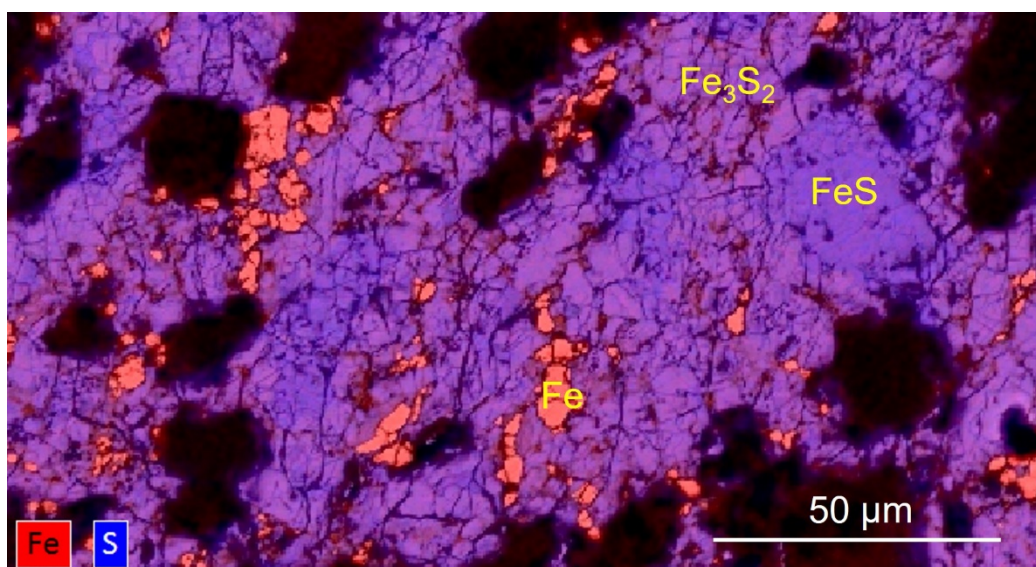
175 Figure 1. (a) Angle dispersive XRD patterns collected on Fe-15S upon heating at ~14 GPa. Peaks
 176 of NaCl and BN are observed all the time. Reflections from FeO appeared at 780 K and remained
 177 visible over the entire explored P-T range. Diffraction signal of Fe₃S₂ appeared at 890 K and
 178 disappeared upon melting, once the diffuse signal was detected. The phase transition from hcp-Fe
 179 to fcc-Fe was observed between 890 K and 1049 K. The partially molten sample at 1109 K only
 180 shows diffuse signal from liquid and sharp peaks from fcc-Fe. (b) Angle dispersive XRD patterns
 181 collected along the full experimental path for the run on Fe-20S. An almost isobaric heating (from
 182 780 K to 940 K) was followed by an isothermal decompression (from 14 GPa to 12.1 GPa at 940
 183 K). For clarity, the diffraction peaks of each component are annotated only upon their initial
 184 appearance. The peaks belonging to Fe₃S₂ are highlighted by the dashed boxes.

185

186 The EDS mapping of the recovered Fe-25S shown in Figure 2 clearly indicates that
 187 the sample contains two different Fe-S compounds together with a small amount of
 188 iron, which came from the partial decomposition of Fe₃S₂ during quench. EDS
 189 analysis were conducted on the three phases, and the results are shown in Table 2. The
 190 deviation of the atomic percent of S from the theoretical value in Fe₃S₂ and FeS was
 191 ascribed to the partial Fe₃S₂ decomposition, with produced grain size likely smaller
 192 than the beam size (2 μm).

193

194



195

196

197 Figure 2. EDS mapping of Fe-25S. Fe, Fe_3S_2 , and FeS are identified by different colors. Fe was
 198 not observed in diffraction pattern before quench, indicating that Fe_3S_2 was partially decomposed
 199 during quench. The dark regions, which are hollows, correspond to the detached NaCl (pressure
 200 marker) grains during polishing.

201

202

203 Table 2 EDS quantification on the phases of recovered Fe-25S

Phase	O	S	Fe	Total*
Fe	0 (0)	0.16 (0.06)	99.84 (0.11)	100.00
Fe_3S_2	1.94 (0.54)	41.56 (1.63)	56.50 (1.84)	100.00
FeS	0.11(0.25)	46.26 (1.26)	53.63 (1.42)	100.00

204 Note: Standardless EDS analysis, the content has been rescaled and is shown in
 205 atomic percent.

206

207

208 3.2 Stability field and structure of Fe_3S_2

209

210 Among the high-temperature runs in the 12-14 GPa range, three of them were
 211 quenched right after the completion of the phase transition, above ~ 900 K, so to keep
 212 the phase, while Fe-15S was heated till partial melting. As mentioned above, new
 213 peaks of Fe_3S_2 emerged around 870 K in all these runs (the exact temperature at
 214 which Fe_3S_2 emerged can be found in Table S1). On the contrary Fe_3S_2 was not
 215 observed in the low-pressure run on Fe-25S from 11 GPa at ambient temperature until
 216 sample melting at 1100 K and 12 GPa, providing a low-pressure boundary to the
 217 Fe_3S_2 phase stability. The phase transition boundary was confirmed by the isothermal
 218 decompression on Fe-20S at 940 K, with Fe_3S_2 found to start decomposing at 12.2
 219 GPa. Right panel of Figure 1 shows the diffraction patterns collected along the entire
 220 experimental P-T path of the Fe-20S run. Similar to the case of Fe-15S, the new peaks
 221 belonging to Fe_3S_2 and highlighted in the dashed boxes were detected at 900 K also in

222 this run, with the simultaneous disappearance of peaks from FeS and hcp-Fe. In this
223 run the appearance of Fe₃S₂ coincides with the hcp-fcc transition of iron (Klotz et al.,
224 2008), so that the remaining iron adopted the fcc structure, retained till the end of the
225 run. The FeS phase was observed again below 12.2 GPa in concomitance with the
226 disappearance of the new peaks, clear indication of the decomposition of Fe₃S₂. NaCl,
227 serving as the pressure calibrant, was detectable during the whole experiment, as is
228 the signal from the hBN capsule.

229

230 On the other hand, the run on Fe-15S indicates that the Fe₃S₂ is stable until the onset
231 of melting, and that the peaks of Fe₃S₂ disappeared simultaneously with the
232 appearance of the diffused signal from the melt (Figure 1). This is in good agreement
233 with the phase diagram inferred by Fei et al. (1997).

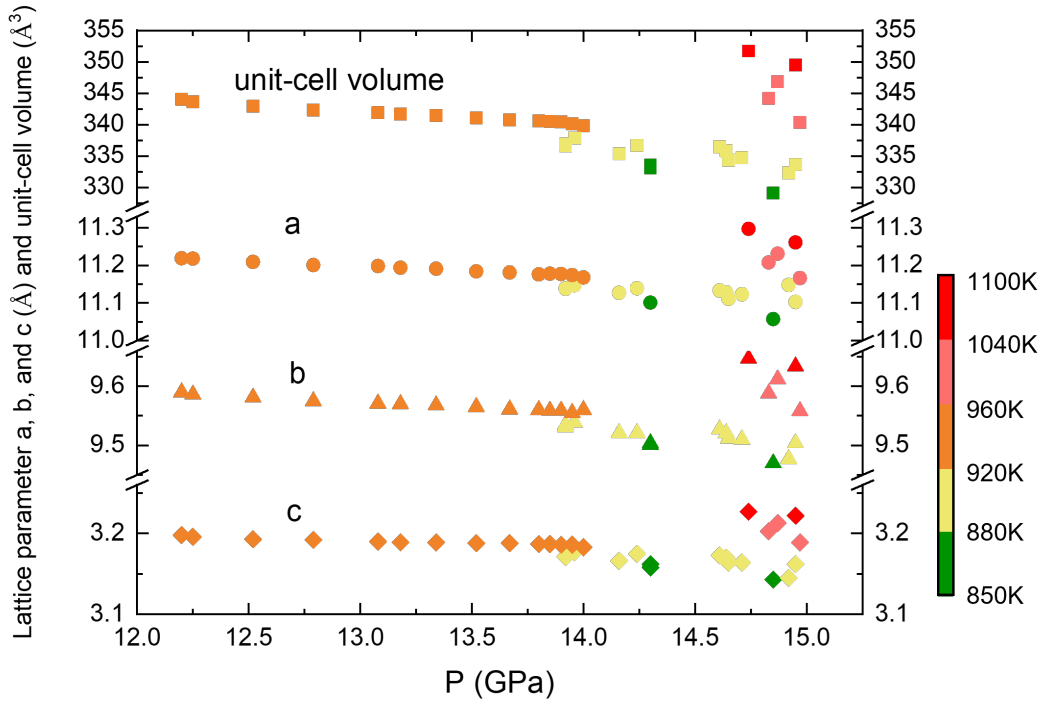
234

235 Rietveld refinement was conducted by GSAS-II (Toby and Von Dreele, 2013) to
236 extract the peaks of Fe₃S₂ (Figure S3). The crystal structure was then determined, and
237 the lattice was indexed using DICVOL based on 29 observed reflections (peak
238 position and intensity provided in Table 3). Unlike previous reports on quenched
239 samples suggesting either monoclinic or triclinic structure (Fei et al., 1997;
240 Koch-Müller et al., 2002), our crystallographic analysis indicate that Fe₃S₂ adopts an
241 orthorhombic structure. We believe this different conclusion is a consequence of the
242 improved quality of the diffraction patterns made possible by the enhanced
243 performances of the beamline and the upgraded synchrotron source. Indeed, thanks to
244 the new storage ring (ESRF - Extremely Brilliant source) and the new setup of the
245 ID27 beamline, the signal-to-noise ratio of the diffraction patterns has been
246 remarkably improved, allowing us the identification of many minor reflections and
247 solving peak overlaps (see Figure S3).

248

249 The derived lattice parameters and the unit-cell volume at the experimental P-T
250 conditions from all the runs, and irrespectively of the starting powder composition,
251 are plotted in Figure 3 and provided in Table S1.

252



253

254 Figure 3. Lattice parameters and unit-cell volume of Fe_3S_2 as a function of pressure in the
 255 temperature range from 850 K to 1100 K (color coded). Squares represent the unit-cell volumes
 256 (in \AA^3), while circles, triangles, and diamonds are the values of lattice parameter a, b, and c,
 257 respectively (in \AA). Errors are smaller than the symbols.

258 Table 3 Observed diffraction pattern and calculated d values of Fe-20S at 12.8 GPa and 940 K

h	k	l	d_{OBS} (\AA)	I_{OBS} (a.u.)	d_{CAL} (\AA)
2	0	0	5.606	0.2	5.601
1	0	1	3.071	0.5	3.070
0	1	1	3.029	2.3	3.029
3	2	0	2.943	1.9	2.944
4	0	0	2.801	0.4	2.801
4	1	0	2.688	1.4	2.688
2	1	1	2.665	0.3	2.664
2	2	1	2.400	2.5	2.400
3	1	1	2.352	2.7	2.352
1	4	0	2.341	2.4	2.341
0	3	1	2.257	0.6	2.257
2	4	0	2.201	1.8	2.201
5	1	0	2.182	3.0	2.182
3	2	1	2.164	2.2	2.164

4	3	0	2.105	7.0	2.105
2	3	1	2.093	14.1	2.093
3	4	0	2.015	5.0	2.015
3	3	0	1.931	0.5	1.932
1	5	0	1.888	4.8	1.888
6	0	0	1.867	0.9	1.867
2	5	0	1.812	0.9	1.812
5	1	1	1.801	2.5	1.801
4	3	1	1.757	2.1	1.757
5	2	1	1.713	1.6	1.713
3	5	0	1.704	1.8	1.704
0	5	1	1.642	0.7	1.642
1	5	1	1.625	0.4	1.625
6	3	0	1.611	4.1	1.612
0	6	0	1.596	6.2	1.596

259

260

261 3.3 Estimated density of Fe₃S₂ and number of atoms in the unit cell

262

263 Due to the peaks' overlap and broadening of the powder diffraction pattern, it was not
 264 possible to determine the space group and coordination number of Fe₃S₂ and,
 265 consequently, its density. However, a reasonable estimate on the density can be made
 266 starting from the density of the reactants, Fe and FeS, assuming no significant volume
 267 change during the following reaction:

268



269

270

271 Using the density of fcc-iron (8334 kg/m³) and FeS (5841 kg/m³) extracted from the
 272 run of Fe-20S at 940 K and 14 GPa, where the diffraction peaks of fcc-iron, FeS, and
 273 Fe₃S₂ were all detected, the density of Fe₃S₂ is estimated in ~ 6295 kg/m³.

274 The density is related to the unit-cell volume and the molar mass by the relation:

275

276

$$\rho = \frac{M}{V_{\text{unit-cell}} \times N_A / Z}$$

277

278 where $V_{\text{unit-cell}}$ is the unit-cell volume, M the molar mass, N_A the Avogadro
 279 number, and Z the number of atoms in a unit cell. Crystals commonly have even Z
 280 values. With hypothetic Z values of 2, 4, 6, 8, and 12, the resulting densities of Fe₃S₂
 281 would be 2264, 4528, 6792, 9056, and 13585 kg/m³, respectively. Therefore, $Z=6$
 282 seems to be the most probable solution, since it provides the least positive mismatch
 283 with respect to the density estimated from the reactants.

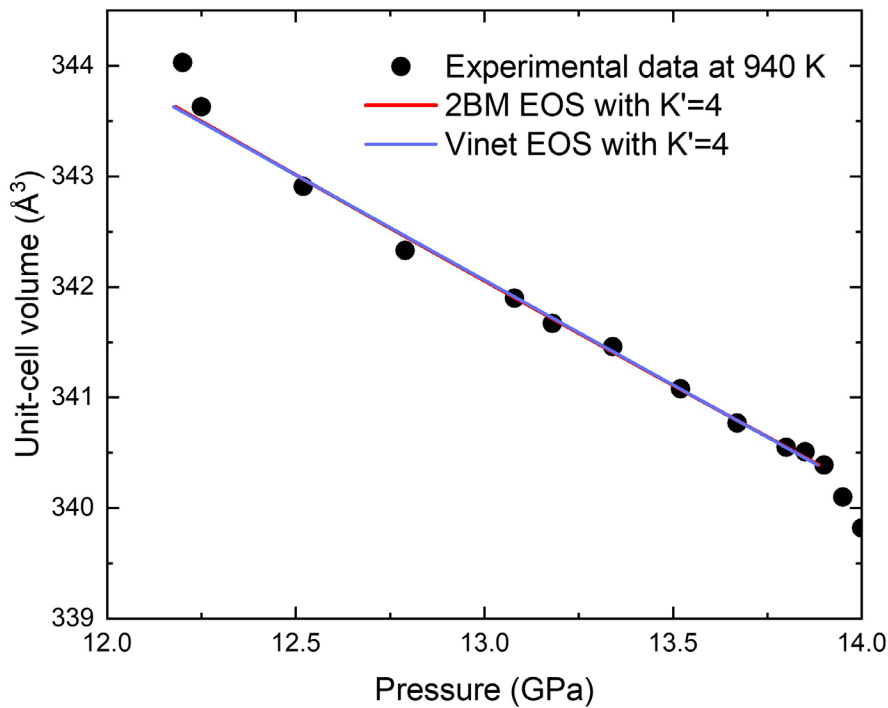
284 3.4 Thermo-elastic properties of Fe₃S₂

285

286 As Fe₃S₂ decomposes to Fe + FeS below 12.2 GPa, and melts above 1100 K,
287 structural information on Fe₃S₂ can be obtained only in a relatively narrow P-T range.
288 The collected isothermal decompression data allow to determine the isothermal bulk
289 modulus K at 940 K, but the small pressure range does not permit the reliable
290 assessment of its pressure derivative K' . As such, the data points were fitted to a
291 second-order Birch-Murnaghan equation of state (2BM-EOS) as well as to a Vinet
292 formalism with K' fixed to 4. As shown in Figure 4, the two fits equally well account
293 for the data and are essentially indistinguishable. The resulting parameters are listed
294 in Table 4. We note however that the obtained bulk modulus and the zero-pressure
295 volume (parameters correlated in the fits) are different depending on the used
296 formalism, with 2BM-EOS providing larger initial volume and larger compressibility,
297 while the fit to a Vinet formalism yields smaller initial volume and, consequently,
298 smaller compressibility. A bulk modulus of either 130 GPa (2BM-EOS) or 185 GPa
299 (Vinet) falls in the range of values reported for hcp-Fe (Hirao et al., 2022),
300 tetragonal-Fe₃S (Fei et al., 2000) and cubic-FeS₂ (Thompson et al., 2016), while we
301 observe that the bulk modulus of hexagonal-FeS-IV is much lower (Urakawa et al.,
302 2004).

303 In spite of the limited temperature range (850 K to 1100 K), data around 14-15 GPa
304 allowed estimation of the thermal expansion as $26.6 \times 10^{-5} \text{ K}^{-1}$ (Table 4).

305



306

307 Figure 4. Experimental data and fitted EOS for K' fixed to 4. A few points at the two ends of the

308 here-considered pressure range have not been considered in the fitting procedure as they showed a
 309 variance in the volume related to the approaching phase boundary.

310

311

312 Table 4. Fitted thermal expansivity and EOS parameters according to a second-order
 313 Birch-Murnaghan and Vinet formalism with $K'=4$ for Fe_3S_2 at $T = 940$ K.

T_0 (K)	940 K	
Formalism	2 nd -order Birch-Murnaghan	Vinet
$V_{0(T_0)}$ (\AA^3)	372.2 (0.8)	367.3 (0.6)
$K_{0(T_0)}$ (GPa)	130(4)	185 (4)
K'_{T_0}	4 ^a	4 ^a
α ($\times 10^{-5} \text{K}^{-1}$)	26.6 ^b	

314 ^aFixed value.

315 ^bThe value is determined by the definition of thermal expansion based on the experimental
 316 volumes in the range of 14-15 GPa and 850-1100 K.

317

318 It is worth noting that the here-estimated thermal expansivity of Fe_3S_2 is higher than
 319 that reported for Fe (Komabayashi, 2014) and FeS (Urakawa et al., 2004), which
 320 conversely are relatively close. The axial thermal expansion coefficients are shown in
 321 Table 5 in comparison with those determined for Fe and FeS (all data are from this
 322 study). In all cases we note a slightly larger thermal expansivity along the c-axes and,
 323 above all, the larger thermal expansivity of Fe_3S_2 along all directions. Being thermal
 324 expansivity of FeS and Fe relatively close, we tend to believe that S alloying does not
 325 pay a major role (a clear compositional dependence of thermal expansion was not
 326 reported neither in the case of liquid Fe-S alloys at high pressure, see Xu et al., 2021)
 327 and that the larger thermal expansivity of Fe_3S_2 is rather related to atomic
 328 arrangement, with the orthorhombic structure more sensible to the effect of
 329 temperature than the hexagonal structure.

330

331 Table 5. Thermal expansivity of hcp-Fe, Fe_3S_2 , and FeS

	Crystal system	Pressure range (GPa)	Temperature range (K)	Volumetric α (10^{-5}K^{-1})	Linear α along a (10^{-5}K^{-1})	Linear α along b (10^{-5}K^{-1})	Linear α along c (10^{-5}K^{-1})
hcp-Fe	Hexagonal	14-15	780-920	6.54	1.68	1.68	3.13
Fe_3S_2	Orthorhombic	14-15	850-1100	26.58	8.59	7.41	10.54
FeS-IV	Hexagonal	14-15	520-910	5.27	1.25	1.25	2.75

332

333

334 3.5 Compression behavior of FeS-IV and FeS-V

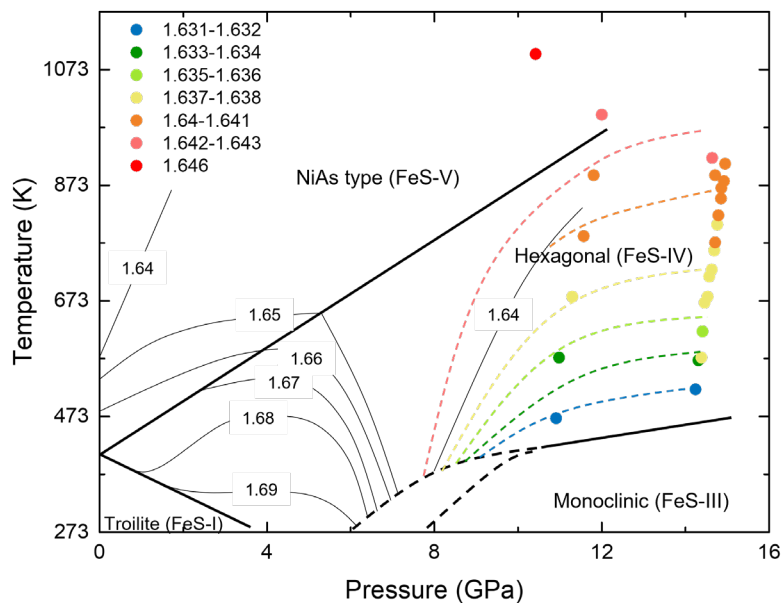
335

336 FeS-IV (hexagonal) and FeS-V (NiAs type) have been observed in both low-pressure

337 and high-pressure runs on Fe-25S and in the run on Fe-30S. The lattice parameters
 338 measured for the two FeS phases are listed in Table S2 using a fundamental NiAs type
 339 cell (a_f and c_f) to describe the unit cell of these two phases, where $a = 2a_f$ and
 340 $c = c_f$ for FeS-IV, and $a = a_f$ and $c = c_f$ for FeS-V (Kusaba et al., 1998).

341

342 All the FeS phases show an anisotropic compressibility tracked by the evolution of
 343 the c_f/a_f ratio with temperature and pressure. The pressure range from 0 to 8 GPa
 344 was already carefully investigated by Kusaba et al. (1998) and the derived
 345 dependence of c_f/a_f ratio with pressure and temperature is shown in Figure 5
 346 together with our data on FeS-IV and FeS-V at higher pressure and high temperature.
 347 Our results show a high consistency with the previous work and complement
 348 published dataset with further data at higher pressures and temperatures.



349

350 Figure 5. Contours of c_f/a_f ratio of FeS as a function of pressure and temperature between room
 351 temperature and 1173 K and from 0 to 16 GPa. The bold black lines indicate the phase boundaries,
 352 and the thin black curves the contours of the c_f/a_f ratio discretized in the range from 1.64 to
 353 1.69 (Kusaba et al., 1998). Colored points are data from the present study, and the dashed curves
 354 with same color are estimated contours. Reported the c_f/a_f contours are also consistent with
 355 those from Urakawa et al., 2004.

356

357

358 4. Discussion

359

360 The stability field of Fe_3S_2 below melting observed in this study confirms the notion
 361 that this phase would be one of the possible phases comprising the solid cores of
 362 medium-sized terrestrial planets and exoplanets, specifically if sulfur-rich. On the
 363 Fe-rich side, this study has defined the temperature range and lower pressure
 364 boundary for the stability field of $\text{Fe}+\text{Fe}_3\text{S}_2$ assemblage (850 K to 1100 K, from 12
 365 GPa). As this phase assemblage is reported by Fei et al. (2000) to evolve into $\text{Fe}+\text{Fe}_3\text{S}$

366 from ~21 GPa, Fe₃S₂ is a pertinent core component of the planetary objects with a
367 metallic core encompassing the (narrow) pressure range from 12 to 21 GPa. For
368 instance, if it is found in a meteorite, the Fe₃S₂ phase provides tight constraints on the
369 size and temperature of the parent body.

370

371 More in general, any iron-sulfur core model in the range 12-21 GPa should correctly
372 account for the stability of Fe₃S₂. At subsolidus temperature, Fe₃S₂ should be used as
373 end-member phase in thermodynamic models together with, respectively, Fe or FeS
374 depending on whether the S content is below or above 27 wt%. Crystallization
375 scenarios largely rely on the core bulk sulfur concentration. If the core composition is
376 on Fe-rich side of the Fe-FeS system (e.g. at 14 GPa S <18 wt.% according to Fei et
377 al., 1997), iron would first crystallize, resulting in either iron snow or growing of an
378 iron inner core from the planetary center depending on the relative slope of the
379 liquidus vs. the adiabat. In both cases, Fe₃S₂ would appear only upon further cooling,
380 at the last stages of the core crystallization, forming a less-dense solid layer
381 surrounding the iron inner core. Conversely, a core with a composition on the
382 sulfur-rich side of Fe-FeS system (e.g. at 14 GPa a bulk sulfur content >21 wt.%
383 according to Fei et al., 1997) would experience at first the crystallization of FeS, and
384 Fe₃S₂ would stabilize only around solidus temperature. Fe₃S₂ would be the first solid
385 phase to crystallize only for bulk sulfur content between 18 and 21 wt.%, which
386 clearly narrow down the likelihood of this event. In addition, despite the fact that
387 Fe₃S₂ is less dense than the coexisting liquid and would therefore tend to float up to
388 the core-mantle boundary, the resulting crystallized core would be less markedly
389 stratified because of the small temperature difference between solidus and liquids.
390 Ultimately, compared to Fe and FeS, Fe₃S₂ is a low-temperature candidate of
391 planetary core materials, relevant in particular for entirely solid cores or cores towards
392 the end of their crystallization process.

393

394 These general considerations are further developed here below in the cases of the core
395 of selected planetary bodies within the solar system.

396

397 Gravity measurements collected by the Galileo mission have been used to construct a
398 range of interior structure and composition models for the Galilean satellites of Jupiter
399 (Anderson et al., 1996a, 1996b, 1998, 2001; Sohl et al., 2002). Although current
400 understanding of the interiors of Europa, Io, and Ganymede is quite limited, all
401 models point at a metallic core, and none foresee a central pressure exceeding 11 GPa.
402 As such, the main solid products of a crystallizing Fe-S core would be Fe or FeS,
403 depending on sulfur concentration, and not Fe₃S₂. However the stabilization of Fe₃S₂
404 already at 12 GPa and not at 14 GPa as previously assumed (e.g. Hauck et al., 2006;
405 Breuer et al. 2015) has important consequences on the thermodynamic modeling and
406 thermal evolution models, specifically in the case of Ganymede, whose central
407 pressure approaches 11 GPa (Sohl et al., 2002). Indeed, the evolution of the eutectic
408 temperature with pressure changes its slope, from negative to positive in
409 concomitance to the stabilization of Fe₃S₂. Refined melt relations are expected to have

410 implications on the crystallization regime, which directly reflects into mechanism for
411 dynamo generation (Hauck et al., 2006; Breuer et al. 2015; Rückriemen et al., 2015,
412 2018). Compositional-driven convection is the preferred mechanism for driving the
413 dynamo responsible for the Ganymede's magnetic field (Hauck et al. 2006; Bland et
414 al. 2008) and a proper modeling heavily relies on the accurate knowledge of the phase
415 diagram, in particular of the melting temperatures as a function of bulk sulfur content,
416 and thermo-elastic properties of stable phases. Additional magnetic and geodetic data
417 concerning the Galilean satellites of Jupiter will come thanks to the Juno flybys over
418 the extended mission and, above all, the ESA JUICE and NASA Europa Clipper
419 missions. In this context, our work, which refines the Fe-S phase diagram and
420 provides the thermo-elastic properties of the Fe_3S_2 phase, is particularly timely.

421

422 Two telluric planets in the solar system whose core encompasses the pressure range of
423 stability of the Fe_3S_2 phase are Mercury and Mars.

424

425 Mercury has a very large, partially molten core (Margot et al., 2007), with the
426 pressure spanning from 5-8 GPa at core mantle boundary (CMB) to 30-44 GPa at the
427 center (Rivoldini et al., 2009). The most recent models based on geodetic data require
428 the presence of a large solid inner core, likely no smaller than 1000 km in radius
429 (Genova et al., 2019; Steinbrügge et al., 2021). Silicon, carbon, and sulfur are three
430 favored light elements present in the Mercury's core (Namur et al., 2016; Steenstra
431 and van Westrenen, 2020; Steenstra et al., 2020). Considering the high incompatibility
432 of sulfur in solid iron when silicon is present (e.g. Chabot et al., 2014) and the
433 recently established melting relation in the Fe-Si-C system (Miozzi et al., 2022), a
434 Fe-Si phase would be the first phase to crystallize to form an inner core, with a
435 structure highly depending on the actual Si content (Edmund et al. 2022). The
436 accreting inner core would also contain carbon along with Fe and Si, up to the
437 solubility limit, leaving a liquid outer core essentially made by Fe-S (in case C
438 content overcomes the solubility limit in the Fe-Si phase, formed carbides or
439 diamonds would float and accumulate at the CMB, eventually transforming into
440 graphite and moving to the crust, see discussion in Miozzi et al., 2022). As such, the
441 Fe-S system still provides a reference to assess the properties of Mercury's liquid
442 outer core. (e.g. Hauck et al., 2007; Rivoldini et al., 2009; Dumberry and Rivoldini
443 2015; Genova et al., 2019). When considering current estimates of the plausible sulfur
444 content in the liquid outer core, spanning from ~5-6 wt% advocated on the basis of
445 geodetic constraints (Steinbrügge et al., 2021), down to less than 1.5 wt% based on
446 geochemical considerations (Namur et al., 2016), iron would be the first solid phase to
447 crystallize upon further cooling of the Fe-S liquid core. As such, as the inner core
448 grows, the outer core becomes progressively richer in sulfur, reaching the value of
449 ~11.3-13.7 wt% (for an initial concentration of 5-6 wt%) or 3.5 wt% (for an initial
450 concentration of 1.5 wt%) for a solid core of 1700 km in radius (corresponding to 12
451 GPa at the inner-core outer-core boundary, based on the pressure profile in
452 Steinbrügge et al., 2021). Under the assumption that the pressure profile of Mercury
453 only marginally changes during the inner core growing, the sulfur content in the liquid

454 outer core would still be not enough to enable the crystallization of Fe₃S₂.

455

456 Core-mantle boundary on Mars is currently estimated in the 18-20 GPa range (Stähler
457 et al., 2021; Irving et al., 2023; Samuel et al., 2023), but its core is most likely fully
458 molten (Irving et al., 2023; Le Maistre et al., 2023). Irrespectively of the possible
459 presence of a molten silicate layer atop the liquid Martian core (e.g. Samuel et al.,
460 2023), estimated densities are such to call for more than 20 wt% S when modeling the
461 core in the Fe-FeS binary system, thus placing this composition on the S-rich side of
462 the Fe-FeS phase diagram in the pressure range 18-40 GPa (Mori et al., 2017). Upon
463 secular cooling, depending on the depth at which crystallization begins, S-rich phases
464 such as Fe₃S, Fe₂S, and Fe₃S₂ would all be possibly produced. In particular, Fe₃S₂
465 could crystallize close to the core-mantle boundary for a liquid core with S in the
466 range 15-25 wt% as indicated by the Fe-FeS phase diagram at 21 GPa (Fei et al.,
467 2000). We stress, however, the low temperatures near the eutectic (e.g., 1100°C at 21
468 GPa by Fei et al., 2000) are needed for this to occur, making this event possible to
469 occur only in the far future.

470

471 5. Conclusions

472

473 Properties of Fe₃S₂, including phase stability, structure, lattice parameters and
474 equation of state were studied by *in situ* X-ray diffraction between 11 and 15 GPa and
475 up to the partial-melting temperature of 1100 K. *In situ* measurements were
476 complemented by SEM and EDS analysis of the recovered samples. Fe₃S₂ was
477 observed thermodynamically stable above 12.1 GPa at 850 K, adopting an
478 orthorhombic crystalline structure. In the binary Fe-S system, it coexists with Fe or
479 FeS depending on the sulfur bulk concentration, and it is stable till melting. Analysis
480 of the diffraction patterns allowed determination of the lattice parameters and of the
481 unit-cell volume at all the P-T conditions where Fe₃S₂ was observed, without
482 noticeable difference from run to run. Fitting the isothermal data collected for a
483 reference temperature of 940 K to a second-order Birch-Murnaghan and a Vinet
484 equation of state with K' fixed to 4 yields zero-pressure volume V_0 of 372.2 ± 0.8
485 and $367.3 \pm 0.6 \text{ \AA}^3$, with zero-pressure bulk modulus K_0 of 129.9 ± 3.8 and 185.2
486 ± 4.0 GPa, respectively. The two formalisms equally well fit the dataset. Based on the
487 unit-cell volume collected from 850 K to 1110 K at around 14 GPa, the thermal
488 expansion, assumed constant in this P-T range, was determined to be $26.6 \times 10^{-5} \text{ K}^{-1}$.

489

490 Within this study we also determined the lattice parameters and compressional
491 behavior of FeS from 11 to 15 GPa between 470 K and 1100 K, in both hexagonal and
492 NiAs-type structure. We extracted reliable c_f/a_f ratio of FeS from all the runs and
493 depicted the dependence on pressure and temperature, extending on previous data.

494

495 Being stable till melting, Fe₃S₂ could crystallize upon secular cooling of S-rich cores
496 of terrestrial planets or exoplanets. In particular, any solid iron-sulfur core model in
497 the 12-21 GPa range should use Fe₃S₂ as end member with, respectively, Fe or FeS

498 depending on whether the S content is below or above 27 wt.%. Another direct
499 implication of the Fe₃S₂ stability field determined in this study for core modeling
500 concerns the pressure dependence of the eutectic temperature, which decreases with
501 increasing pressure until Fe₃S₂ stabilizes and increases thereafter. Such a change in
502 the slope should be placed at 12 GPa and not at 14 GPa as assumed so far (e.g.
503 Stewart et al., 2007; Breuer et al. 2015; Dumberry and Rivoldini 2015).

504

505 The relatively narrow stability field of Fe₃S₂ is such that it is not expected to be stable
506 within the core of the Galilean satellites of Jupiter, Europa, Io, and Ganymede, whose
507 central pressure should not exceed 11 GPa and which would thus crystallize either Fe
508 or FeS depending on bulk S content. Crystallization of Fe₃S₂ is also not likely in the
509 case of Mercury, which, although having a core encompassing the relevant pressure
510 range, should not have the required S content. In a far future, upon secular cooling,
511 Martian core could crystallize Fe₃S₂ close to its core-mantle boundary around the
512 eutectic temperature of Fe-S alloy.

513

514 Iron sulfides are commonly found in many classes of meteorites (e.g. Jones and Drake,
515 1983; Fei et al., 1995; Scott 2011). If Fe₃S₂ were found in a meteorite, this would
516 provide tight constraints on the size and temperature of the parent body and/or the
517 experienced shock conditions. Indeed, Fe₃S₂ is not expected to be observed in pristine
518 iron meteorites originating from the asteroids belt due to their reduced dimensions and
519 consequent low pressure, and its eventual presence would be a consequence of the
520 P-T conditions experienced during impacts. On the other end, meteorites can also be
521 generated from highly energetic events, leading to explosions of larger planetary
522 bodies. In this context, a meteorite containing Fe₃S₂ would be indicative of a parent
523 body whose core would have a minimal pressure of 12 GPa, but no more than 21 GPa.

524

525

526

527 Data availability statement

528 Raw XRD experimental data have been published in the Zenodo online repository (B.
529 Zhao et al., 2023).

530

531 Acknowledgements

532

533 We thank Omar Boudouma for his help with SEM and EDS analysis at IStEP. We also
534 thank Gaston Garbarino for the technical supports during the beamtime at ESRF. We
535 thank Xie Longjian for his help with a test run at BL04B1 beamline in SPring-8
536 (under proposal 2023A1109). This project has received funding from the European
537 Research Council (ERC) under the European Union's Horizon 2020 research and
538 innovation Programme (grant number 724690). The authors acknowledge ESRF for
539 the provision of beamtime under proposal ES-1145.

540

541

542 References

543

544 Anderson, J.D., Sjogren, W.L. and Schubert, G., 1996a. Galileo gravity results and the internal
545 structure of Io. *Science* 272, 709-712. <https://doi.org/10.1126/science.272.5262.709>.

546

547 Anderson, J.D., Lau, E.L., Sjogren, W.L., Schubert, G., Moore, W.B., 1996b. Gravitational
548 constraints on the internal structure of Ganymede. *Nature* 384, 541-543.
549 <https://doi.org/10.1038/384541a0>.

550

551 Anderson, J.D., Schubert, G., Jacobson, R.A., Lau, E.L., Moore, W.B., Sjogren, W.L., 1998.
552 Europa's differentiated internal structure: Inferences from four Galileo encounters. *Science* 281,
553 2019-2022. <https://doi.org/10.1126/science.281.5385.201>.

554

555 Anderson, J.D., Jacobson, R.A., Lau, E.L., Moore, W.B., Schubert, G., 2001. Io's gravity field and
556 interior structure. *J. Geophys. Res., Planets* 106, 32963-32969.
557 <https://doi.org/10.1029/2000JE001367>.

558

559 Antonangeli, D., Morard, G., Schmerr, N.C., Komabayashi, T., Krisch, M., Fiquet, G., Fei, Y.,
560 2015. Toward a mineral physics reference model for the Moon's core. *Proc. Natl. Acad. Sci.*
561 *USA* 112, 3916–3919. <https://doi.org/10.1073/pnas.1417490112>.

562

563 Bland MT, Showman AP, Tobie G., 2008. The production of Ganymede's magnetic field. *Icarus*
564 198, 384–399. <https://doi.org/10.1016/j.icarus.2008.07.011>.

565

566 Boulard, E., Denoual, C., Dewaele, A., King, A., Le Godec, Y., Guignot, N., 2020. Following the
567 phase transitions of iron in 3D with X-ray tomography and diffraction under extreme
568 conditions. *Acta Mater.* 192, 30-39. <https://doi.org/10.1016/j.actamat.2020.04.030>.

569

570 Boultif, A., Louër, D., 1991. Indexing of powder diffraction patterns for low-symmetry lattices by
571 the successive dichotomy method. *J. Appl. Crystallogr.* 24, 987-993.
572 <https://doi.org/10.1107/S0021889891006441>.

573

574 Breuer, D., Rueckriemen, T., Spohn, T., 2015. Iron snow, crystal floats, and inner-core growth:
575 modes of core solidification and implications for dynamos in terrestrial planets and moons. *Prog.*
576 *Earth Planet. Sci.* 2, 1-26. <https://doi.org/10.1186/s40645-015-0069-y>.

577

578 Bueno, A.S., Walker, D., 2011. The Fe-rich liquidus in the Fe–FeS system from 1 bar to 10 GPa.
579 *Geochim. Cosmochim. Acta* 75, 2072–2087. <https://doi.org/10.1016/j.gca.2011.01.030>.

580

581 Chabot N. L., Wollack E. A., Klima R. L., Minitti M. E., 2014. Experimental constraints on
582 Mercury's core composition. *Earth Planet. Sci. Lett.* 390, 199–208.
583 <https://doi.org/10.1016/j.epsl.2014.01.004>.

584

585 Deng, L., Fei, Y., Liu, X., Gong, Z., Shahar, A., 2013. Effect of carbon, sulfur and silicon on iron

586 melting at high pressure: Implications for composition and evolution of the planetary terrestrial
587 cores. *Geochim. Cosmochim. Acta* 114, 220-233. <https://doi.org/10.1016/j.gca.2013.01.023>.
588

589 Dumberry, M., Rivoldini, A., 2015. Mercury's inner core size and core-crystallization
590 regime. *Icarus* 248, 254-268. <https://doi.org/10.1016/j.icarus.2014.10.038>.
591

592 Edmund, E., Morard, G., Baron, M.A., Rivoldini, A., Yokoo, S., Boccato, S., Hirose, K.,
593 Pakhomova, A., Antonangeli, D., 2022. The Fe-FeSi phase diagram at mercury's core conditions.
594 *Nature Comm.* 13, 387. <https://doi.org/10.1038/s41467-022-27991-9>.
595

596 Fei, Y., Bertka, C.M., Finger, L.W., 1997. High-pressure iron-sulfur compound, Fe₃S₂, and melting
597 relations in the Fe-FeS system. *Science*, 275, 1621-1623.
598 <https://doi.org/10.1126/science.275.5306.1621>.
599

600 Fei, Y., Li, J., Bertka, C.M., Prewitt, C.T., 2000. Structure type and bulk modulus of Fe₃S, a new
601 iron-sulfur compound. *Am. Mineral.* 85, 1830-1833. <https://doi.org/10.2138/am-2000-11-1229>.
602

603 Fei, Y., Prewitt, C.T., Mao, H.K. Bertka, C.M., 1995. Structure and density of FeS at high pressure
604 and high temperature and the internal structure of Mars. *Science* 268, 1892-1894.
605 <https://doi.org/10.1126/science.268.5219.1892>.
606

607 Genova A., Goossens S., Mazarico E., Lemoine F. G., Neumann G. A., Kuang W., Sabaka T. J.,
608 Hauck S. A., Smith D. E., Solomon S. C., Zuber M. T., 2019. Geodetic evidence that mercury has
609 a solid inner core. *Geophys. Res. Lett.* 46, 3625–3633. <https://doi.org/10.1029/2018GL081135>.
610

611 Hauck, S.A., Aurnou, J.M., Dombard, A.J., 2006. Sulfur's impact on core evolution and magnetic
612 field generation on Ganymede. *J. Geophys. Res., Planets* 111, E09008,
613 <https://doi.org/10.1029/2005JE002557>.
614

615 Hauck, S.A., Solomon, S.C., Smith, D.A., 2007. Predicted recovery of Mercury's internal structure
616 by MESSENGER. *Geophys. Res. Lett.* 34. <https://doi.org/10.1029/2007GL030793>.
617

618 Hirao, N., Akahama, Y. and Ohishi, Y., 2022. Equations of state of iron and nickel to the pressure
619 at the center of the Earth. *Matter Radiat. at Extremes* 7, 3. <https://doi.org/10.1063/5.0074340>.
620

621 Hussmann, H., Shoji, D., Steinbrügge, G., Stark, A., Sohl, F., 2016. Constraints on dissipation in
622 the deep interiors of Ganymede and Europa from tidal phase-lags. *Celest. Mech. Dyn. Astron.* 126,
623 131-144. <https://doi.org/10.1007/s10569-016-9721-0>.
624

625 Irving, J.C.E., Lekić, V., Durán, C., Drilleau, M., Kim, D., Rivoldini, A., Khan, A., Samuel, H.,
626 Antonangeli, D., Banerdt, W.B., Beghein, C., Bozdog, E., Ceylan, S., Charalambouss, C., Clinton,
627 J., Davisi, P., Garcia, R., Giardini, D., Horleston, A., Huang, Q., Hurst, K.J., Kawamura, T., King,
628 S.D., Knapmeyer, M., Li, J., Lognonné, P., Maguire, R., Panning, M.P., Plesa, A.-C., Schimmel,
629 M., Schmerr, N.C., Stähler, S.C., Stutzmann, E., Xu, Z., 2023. First observations of core-transiting

630 seismic phases on Mars. *Proc. Natl. Acad. Sci. USA* 120, e2217090120.
631 <https://doi.org/10.1073/pnas.2217090120>.
632
633 Jones, J.H., Drake, M.J., 1983. Experimental investigations of trace element fractionation in iron
634 meteorites, II: The influence of sulfur. *Geochim. Cosmochim. Acta* 47, 1199-1209.
635 [https://doi.org/10.1016/0016-7037\(83\)90062-5](https://doi.org/10.1016/0016-7037(83)90062-5).
636
637 Kivelson, M.G., Khurana, K.K., Russell, C.T., Walker, R.J., Warnecke, J., Coroniti, F.V.,
638 Polansky, C., Southwood, D.J., Schubert, G., 1996. Discovery of Ganymede's magnetic field by
639 the Galileo spacecraft. *Nature* 384, 537-541. <https://doi.org/10.1038/384537a0>.
640
641 Klotz, S., Le Godec, Y., Strässle, T., Stuhr, U., 2008. The α - γ - ε triple point of iron investigated
642 by high pressure-high temperature neutron scattering. *Appl. Phys. Lett.* 93, 091904.
643 <https://doi.org/10.1063/1.2976128>.
644
645 Koch-Müller, M., Fei, Y., Wirth, R., Bertka, C.M., 2002. Characterization of high-pressure
646 iron-sulfur compounds. In: *Lunar and Planetary Science Conference*, 33, 1424.
647
648 Komabayashi, T., 2014. Thermodynamics of melting relations in the system Fe-FeO at high
649 pressure: Implications for oxygen in the Earth's core. *J. Geophys. Res. Solid Earth* 119, 4164-4177.
650 <https://doi.org/10.1002/2014JB010980>.
651
652 Kusaba, K., Syono, Y., Kikegawa, T., Shimomura, O., 1998. High pressure and temperature
653 behavior of FeS. *J. Phys. Chem. Solids* 59, 945-950.
654 [https://doi.org/10.1016/S0022-3697\(98\)00015-8](https://doi.org/10.1016/S0022-3697(98)00015-8).
655
656 Le Maistre, S., Rivoldini, A., Caldiero, A., Yseboodt, M., Baland, R.-M., Beuthe, M., Van Hoolst,
657 T., Dehant, V., Folkner, W. M., Buccino, D., Kahan, D., Marty, J.-C., Antonangeli, D., Badro, J.,
658 Drilleau, M., Konopliv, A., Péters, M.-J., Plesa, A.-C., Samuel, H., Tosi, N., Wieczorek, M.,
659 Lognonné, P., Panning, M., Smrekar, S., Banerdt, W. B., 2023. Spin state and deep interior
660 structure of Mars from InSight radio tracking. *Nature*
661 <https://doi.org/10.1038/s41586-023-06150-0>.
662
663 Margot, J.L., Peale, S.J., Jurgens, R.F., Slade, M.A., Holin, I.V., 2007. Large longitude liberation
664 of Mercury reveals a molten core. *Science* 316, 710-714. <https://doi.org/10.1126/science.1140514>.
665
666 Miozzi, F., Morard, G., Antonangeli, D., Baron, M.A., Pakhomova, A., Clark, A.N., Mezouar, M.,
667 Fiquet, G., 2022. The Fe-Si-C system at extreme P-T conditions: a possible core crystallization
668 pathway for reduced planets. *Geochim. Cosmochim. Acta* 322, 129-142.
669 <https://doi.org/10.1016/j.gca.2022.01.013>.
670
671 Morard, G., Andrault, D., Guignot, N., Sanloup, C., Mezouar, M., Petitgirard, S., Fiquet, G., 2008.
672 In situ determination of Fe-Fe₃S phase diagram and liquid structural properties up to 65
673 GPa. *Earth Planet. Sci. Lett.* 272, 620-626. <https://doi.org/10.1016/j.epsl.2008.05.028>.

674

675 Morard, G., Bouchet, J., Rivoldini, A., Antonangeli, D., Roberge, M., Boulard, E., Denoed, A.,
676 Mezouar, M., 2018. Liquid properties in the Fe-FeS system under moderate pressure: Tool box to
677 model small planetary cores. *Am. Mineral.* 103, 1770-1779.
678 <https://doi.org/10.2138/am-2018-6405>.

679

680 Morard, G., Mezouar, M., Bauchau, S., Álvarez-Murga, M., Hodeau, J.L., Garbarino, G., 2011.
681 High efficiency multichannel collimator for structural studies of liquids and low-Z materials at
682 high pressures and temperatures. *Rev. Sci. Instrum.* 82, 023904.
683 <https://doi.org/10.1063/1.3551988>.

684

685 Morard, G., Mezouar, M., Rey, N., Poloni, R., Merlen, A., Le Floch, S., Toulemonde, P., Pascarelli,
686 S., San-Miguel, A., Sanloup, C., Fiquet, G., 2007. Optimization of Paris–Edinburgh press cell
687 assemblies for in situ monochromatic X-ray diffraction and X-ray absorption. *High Press. Res.* 27,
688 223-233. <https://doi.org/10.1080/08957950601183553>.

689

690 Mori, Y., Ozawa, H., Hirose, K., Sinmyo, R., Tateno, S., Morard, G., Ohishi, Y., 2017. Melting
691 experiments on Fe–Fe₃S system to 254 GPa. *Earth Planet. Sci. Lett.* 464, 135-141.
692 <https://doi.org/10.1016/j.epsl.2017.02.021>.

693

694 Namur, O., Charlier, B., Holtz, F., Cartier, C., McCammon, C., 2016. Sulfur Solubility in reduced
695 mafic silicate melts: Implications for the speciation and distribution of sulfur on Mercury. *Earth
696 Planet. Sci. Lett.* 448, 102–114. <https://doi.org/10.1016/j.epsl.2016.05.024>.

697

698 Ozawa, H., Hirose, K., Suzuki, T., Ohishi, Y., Hirao, N., 2013. Decomposition of Fe₃S above 250
699 GPa. *Geophys. Res. Lett.* 40, 4845-4849. <https://doi.org/10.1002/grl.50946>.

700

701 Pommier, A., Driscoll, P. E., Fei, Y., Walter, M. J., 2022. Investigating metallic cores using
702 experiments on the physical properties of liquid iron alloys. *Front. Earth Sci.* 10, 956971.
703 <https://doi.org/10.3389/feart.2022.956971>.

704

705 Prescher, C., Prakapenka, V.B., 2015. DIOPTAS: a program for reduction of two-dimensional
706 X-ray diffraction data and data exploration. *High Press. Res.* 35, 223-230.
707 <https://doi.org/10.1080/08957959.2015.1059835>.

708

709 Rivoldini, A., Van Hoolst, T., Verhoeven, O., 2009. The interior structure of Mercury and its core
710 sulfur content. *Icarus* 201,12-30. <https://doi.org/10.1016/j.icarus.2008.12.020>.

711

712 Rivoldini, A., Van Hoolst, T., Verhoeven, O., Mocquet, A., Dehant, V., 2011. Geodesy constraints
713 on the interior structure and composition of Mars. *Icarus* 213, 451-472.
714 <https://doi.org/10.1016/j.icarus.2011.03.024>.

715

716 Rückriemen, T., Breuer, D., Spohn, T., 2015. The Fe snow regime in Ganymede's core: A
717 deep-seated dynamo below a stable snow zone. *J. Geophys. Res., Planets* 120, 1095-1118.

718 <https://doi.org/10.1002/2014JE004781>.
719
720 Rückriemen, T., Breuer, D., Spohn, T., 2018. Top-down freezing in a Fe–FeS core and
721 Ganymede’s present-day magnetic field. *Icarus* 307, 172-196.
722 <https://doi.org/10.1016/j.icarus.2018.02.021>.
723
724 Samuel, H., Drilleau, M., Rivoldini, A., Xu, Z., Huang, Q., Garcia, R.F., Lekić, V., Irving, J.C.,
725 Badro, J., Lognonné, P.H. and Connolly, J.A., 2023. Geophysical evidence for an enriched molten
726 silicate layer above Mars’s core. *Nature* 622, 712-717.
727 <https://doi.org/10.1038/s41586-023-06601-8>.
728
729 Scott, E.R.D., 2011. Meteorites: An Overview. *Elements* 7, 47–48.
730 <https://doi.org/10.2113/gselements.7.1.47>.
731
732 Smith, D.E., Zuber, M.T., Phillips, R.J., Solomon, S.C., Hauck, S.A., Lemoine, F.G., Mazarico, E.,
733 Neumann, G.A., Peale, S.J., Margot, J.L., Johnson, C.L., 2012. Gravity field and internal structure
734 of Mercury from MESSENGER. *Science* 336, 214-217. <https://doi.org/10.1126/science.1218809>.
735
736 Sohl, F., Spohn, T., Breuer, D., Nagel, K., 2002. Implications from Galileo observations of the
737 interior structure and chemistry of the Galilean satellites. *Icarus* 157, 104–119.
738 <https://doi.org/10.1006/icar.2002.6828>.
739
740 Stähler, S.C., Khan, A., Banerdt, W.B., Lognonné, P., Giardini, D., Ceylan, S., Drilleau, M., Duran,
741 A.C., Garcia, R.F., Huang, Q., Kim, D., Lekic, V., Samuel, H., Schimmel, M., Schmerr, N.,
742 Sollberger, D., Stutzmann, É., Xu, Z., Antonangeli, D., Charalambous, C., Davis, P.M., Irving,
743 J.C.E., Kawamura, T., Knapmeyer, M., Maguire, R., Marusiak, A.G., M.P. Panning, M.P., Perrin,
744 C., Plesa, A.-C., Rivoldini, A., Schmelzbach, C., Zenhäusern, G., Beucler, É., Clinton, J., Dahmen,
745 N., van Driel, M., Gudkova, T., Horleston, A., Pike, W.T., Plasman, M., Smrekar, S.E., 2021.
746 Seismic detection of the martian core. *Science* 373, 443-448.
747 <https://doi.org/10.1126/science.abi7730>.
748
749 Steenstra, E. S., van Westrenen, W., 2020. Geochemical constraints on core-mantle differentiation
750 in Mercury and the aubrite parent body. *Icarus* 340, 113621.
751 <https://doi.org/10.1016/j.icarus.2020.113621>.
752
753 Steenstra, E.S., Seegers, A.X., Putter, R., Berndt, J., Klemme, S., Matveev, S., Bullock, E.S., Van
754 Westrenen, W., 2020. Metal-silicate partitioning systematics of siderophile elements at reducing
755 conditions: A new experimental database. *Icarus* 335, 113391.
756 <http://doi.org/10.1016/j.icarus.2019.113391>.
757
758 Steinbrügge, G., Dumberry, M., Rivoldini, A., Schubert, G., Cao, H., Schroeder, D.M., Soderlund,
759 K.M., 2021. Challenges on Mercury's interior structure posed by the new measurements of its
760 obliquity and tides. *Geophys. Res. Lett.* 48, e2020GL089895.
761 <https://doi.org/10.1029/2020GL089895>.

762

763 Stewart, A. J., Schmidt, M. W., Van Westrenen, W., & Liebske, C., 2007. Mars: A new
764 core-crystallization regime. *Science* 316, 1323-1325. <https://doi.org/10.1126/science.1140549>.

765

766 Tateno, S., Ozawa, H., Hirose, K., Suzuki, T., I-Kawaguchi, S., Hirao, N., 2019. Fe₂S: The Most
767 Fe-Rich Iron Sulfide at the Earth's Inner Core Pressures. *Geophys. Res. Lett.* 46, 11944-11949.
768 <https://doi.org/10.1029/2019GL085248>.

769

770 Thompson, E.C., Chidester, B.A., Fischer, R.A., Myers, G.I., Heinz, D.L., Prakapenka, V.B.,
771 Campbell, A.J., 2016. Equation of state of pyrite to 80 GPa and 2400 K. *Am. Mineral.* 101, 5,
772 1046-1051. <https://doi.org/10.2138/am-2016-5527>.

773

774 Toby, B.H., Von Dreele, R.B., 2013. GSAS-II: the genesis of a modern open-source all purpose
775 crystallography software package. *J. Appl. Crystallogr.* 46, 544-549.
776 <https://doi.org/10.1107/S0021889813003531>.

777

778 Urakawa, S., Someya, K., Terasaki, H., Katsura, T., Yokoshi, S., Funakoshi, K.I., Utsumi, W.,
779 Katayama, Y., Sueda, Y.I., Irifune, T., 2004. Phase relationships and equations of state for FeS at
780 high pressures and temperatures and implications for the internal structure of Mars. *Phys. Earth
781 Planet. Inter.* 143, 469-479. <https://doi.org/10.1016/j.pepi.2003.12.015>.

782

783 Weber, R.C., Lin, P.Y., Garnero, E.J., Williams, Q., Lognonné, P., 2011. Seismic detection of the
784 lunar core. *Science* 331, 309-312. <https://doi.org/10.1126/science.1199375>.

785

786 Xu, F., Morard, G., Guignot, N., Rivoldini, A., Manthilake, G., Chantel, J., Xie, L., Yoneda, A.,
787 King, A., Boulard, E., Pandolfi, S., Ryerson, F.J., Antonangeli, D., 2021. Thermal expansion of
788 liquid Fe-S alloy at high pressure. *Earth Planet. Sci. Lett.* 563, 116884.
789 <https://doi.org/10.1016/j.epsl.2021.116884>.

790

791 Zhao, B., Morard, G., Boulard, E., Boccato, S., Siersch, N.C., Rivoldini, A., Guignot, N., Henry,
792 L., King, A., Zurkowski, C., Fei, Y., Antonangeli, D., 2023. Local structure and density of liquid
793 Fe-C-S alloys at Moon's core conditions. *J. Geophys. Res., Planets*, e2022JE007577.
794 <https://doi.org/10.1029/2022JE007577>.

795

796 Zhao, B., Morard, G., Boccato S., Mezouar, M., Antonangeli D., 2023. Beamtime ES-1145
797 [Dataset]. Zenodo. <https://doi.org/10.5281/zenodo.7890953>.

798

799 Zurkowski, C.C., Lavina, B., Case, A., Swadba, K., Chariton, S., Prakapenka, V., Campbell, A.J.,
800 2022. Fe₅S₂ identified as a host of sulfur in Earth and planetary cores. *Earth Planet. Sci. Lett.* 593,
801 117650. <https://doi.org/10.1016/j.epsl.2022.117650>.

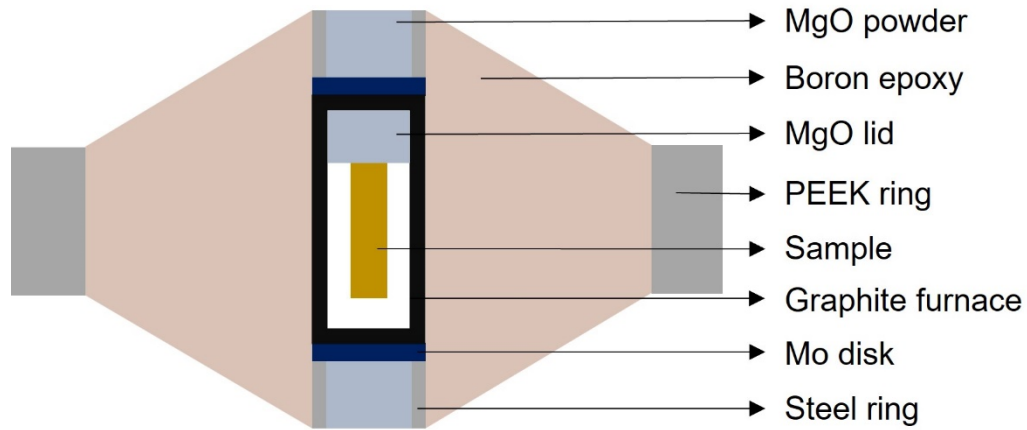
802

803

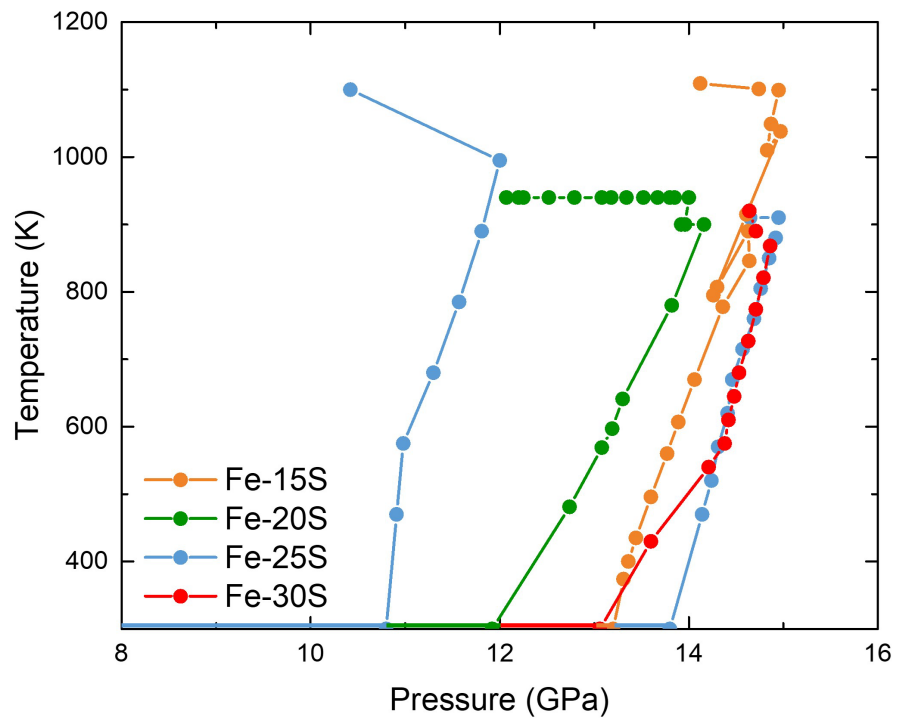
804

805

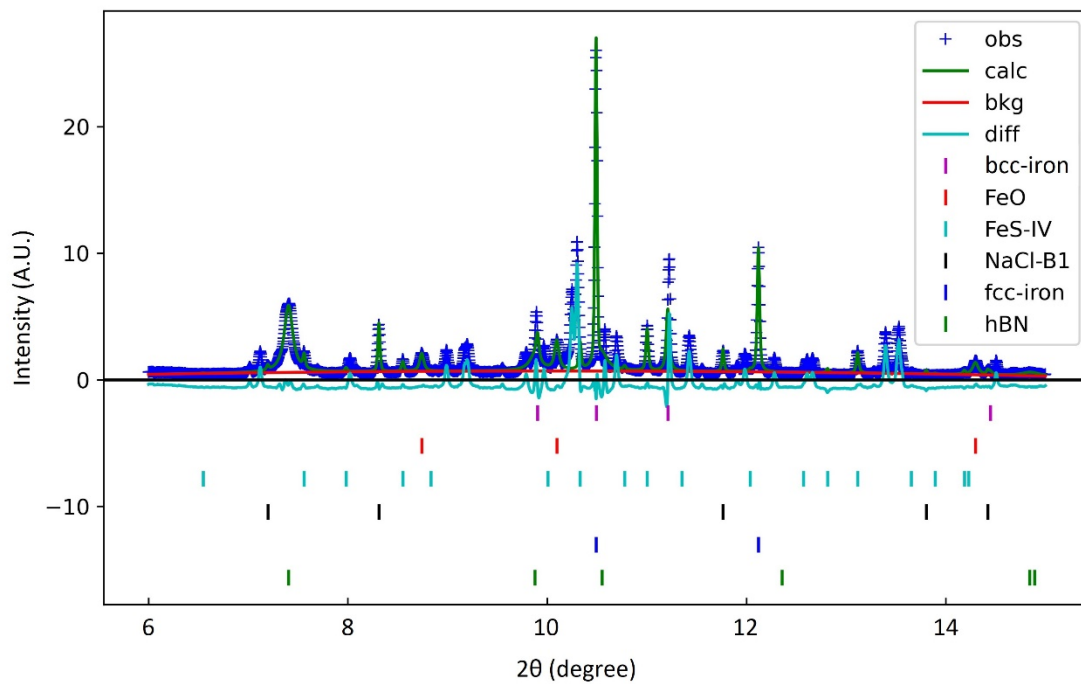
806 Supplementary
807
808 Figure S1-S3
809 Table S1-S2
810
811



812
813 Figure S1 Schematic of the assembly.
814
815



816
817 Figure S2 Experimental P-T paths for five Fe-S samples. All the samples went through a cold
818 compression followed by step heating. The points indicate the P-T conditions where diffraction
819 patterns were collected. All samples were temperature-quenched after the final P-T stage.
820



821

822

823 Figure S3 Rietveld refinement of the diffraction pattern collected on Fe-20S at 13.92 GPa and 900
 824 K. Reflections indexed as FeS and fcc-iron belong to the sample, as FeO, possibly coming from
 825 oxidation of iron in contact with MgO. NaCl was added in the mixture as pressure marker,
 826 chemical reaction between NaCl and Fe-S mixtures was never observed. hBN reflections are from
 827 capsule.

828

829

830

831

832

833

834

835

836

837

838

839

840

841

842

843

844

845

846

847

Runs	P (GPa)	T (K)	a (Å)	b (Å)	c (Å)	V (Å ³)
Fe-15S	14.3	850	11.101	9.501	3.158	333.09
	14.3	850	11.101	9.501	3.162	333.58
	14.61	915	11.133	9.527	3.173	336.49
	14.97	1038	11.166	9.558	3.189	340.33
	14.83	1010	11.208	9.588	3.203	344.15
	14.87	1049	11.231	9.612	3.213	346.84
	14.95	1099	11.261	9.634	3.222	349.50
	14.74	1101	11.297	9.647	3.227	351.71
Fe-20S	14.16	900	11.127	9.521	3.166	335.39
	13.92	900	11.139	9.531	3.171	336.65
	13.92	900	11.138	9.535	3.172	336.92
	13.96	920	11.147	9.539	3.177	337.83
	14.00	940	11.168	9.560	3.183	339.82
	13.95	940	11.174	9.555	3.186	340.1
	13.90	940	11.177	9.559	3.186	340.39
	13.85	940	11.178	9.559	3.187	340.51
	13.80	940	11.176	9.560	3.187	340.55
	13.67	940	11.181	9.561	3.188	340.77
	13.52	940	11.184	9.565	3.188	341.08
	13.34	940	11.191	9.568	3.189	341.46
	13.18	940	11.194	9.570	3.189	341.67
	13.08	940	11.198	9.571	3.190	341.90
	12.79	940	11.201	9.575	3.192	342.33
	12.52	940	11.209	9.581	3.193	342.91
12.25	940	11.218	9.586	3.196	343.63	
12.20	940	11.219	9.590	3.198	344.03	
Fe-25S	14.85	850	11.057	9.470	3.143	329.10
	14.92	880	11.148	9.477	3.145	332.29
	14.95	910	11.103	9.504	3.162	333.64
	14.65	910	11.111	9.512	3.164	334.36

Fe-30S	14.71	890	11.123	9.510	3.164	334.71
	14.64	920	11.128	9.521	3.170	335.86
	14.24	920	11.139	9.521	3.175	336.70

851 Note: Empirical uncertainty on temperature from the cross calibration is ± 100 K and the resulting
852 uncertainty on pressure is ± 0.6 GPa. Uncertainties on lattice parameters and unit-cell volumes are
853 less than the last digit of the data.

854

855 Table S2 Lattice parameters of FeS-IV and FeS-V at experimental P-T conditions

Phase	P (GPa)	T (K)	a, b (Å)	c (Å)	c_f/a_f
Run Fe-25S, low pressure					
	10.91	470	6.537	5.335	1.632
	10.98	575	6.561	5.361	1.634
FeS-IV	11.30	680	6.577	5.185	1.638
	11.57	785	6.593	5.408	1.641
	11.81	890	6.61	5.425	1.641
FeS-V	12.00	995	3.316	5.447	1.643
	10.42	1100	3.349	5.512	1.646
Run Fe-25S, high pressure					
	14.24	520	6.494	5.295	1.631
	14.31	570	6.494	5.303	1.633
	14.41	620	6.499	5.313	1.636
	14.46	670	6.504	5.326	1.638
FeS-IV	14.57	715	6.506	5.327	1.638
	14.69	760	6.512	5.334	1.638
	14.76	805	6.513	5.336	1.638
	14.85	850	6.514	5.338	1.64
	14.92	880	6.519	5.344	1.64
	14.95	910	6.526	5.352	1.64
Run Fe-30S					
	14.38	575	6.43	5.267	1.638
	14.53	680	6.495	5.322	1.638
	14.63	727	6.504	5.328	1.638
FeS-IV	14.71	774	6.513	5.340	1.64
	14.79	821	6.521	5.346	1.64
	14.86	868	6.53	5.356	1.64
	14.71	890	6.544	5.367	1.64

14.64

920

6.530

5.359

1.642

856 Note: Uncertainties same as described below Table S1.

857